Comparison of Finite-State Dynamic Stall Theory with Unsteady Data*

Loren A. Ahaus
Graduate Research Assistant
Department of Mechanical and Aerospace Engineering
Washington University, St. Louis, MO USA

David A. Peters
McDonnell Douglas Professor of Engineering
Department of Mechanical and Aerospace Engineering
Washington University, St. Louis, MO USA

Abstract

Future rotorcraft will incorporate dynamically morphing airfoils, through the use of trailing edge flaps, dynamic camber, dynamic droop, or other methods. In addition, helicopter rotor blades frequently encounter dynamic stall conditions during flight. Currently, dynamic stall is treated using empirical models based on static data for fixed geometry airfoils. Therefore, a unified airloads model is needed that incorporates morphing geometry—as well as dynamic stall—in a state-space framework. This paper presents a unified model that allows the user to compute airloads for an airfoil undergoing arbitrary morphing, using a single set of static data. The linear airloads are calculated using the Peters state-space airloads theory. Then dynamic stall correction is added by adapting the ONERA stall model, applied to the generalized loads. The theory is correlated with wind tunnel testing of a NACA 0012 airfoil with a trailing edge flap, undergoing combined pitch and flap motions. The data include unstalled, moderately stalled, and heavily stalled cases at various phase angles. The theory shows good correlation over a wide range of conditions and correctly captures the character of the lift and moment curves in the dynamic stall regime. The paper also gives a method for computing section characteristics for a morphing airfoil.

*Presented at the 34th European Rotorcraft Forum, Sept. 16-19, 2008, Liverpool, UK.

Nomenclature

a	number of semi-chords the center of rotation is aft of the mid-chord
b	blade semi-chord, m
b_n	induced flow expansion coefficients
$C(k)$	Theodorsen function
C_L	lift coefficient
ΔC_L	static loss of lift
ΔC_n	static loss of nth generalized load
C_M	moment coefficient about the center of rotation
d	number of semi-chords the flap hinge is aft of the mid-chord
f	reversed-flow parameter
$h(x,t)$	generalized airfoil motion, positive down, m
k	reduced frequency of oscillation, $\omega b/u_0$
L	lift per unit span, N/m
L_n	generalized loads per unit span, N/m
$\overline{m}$	camber in NACA xxxx airfoil, *percent chord*
m	$0.01\overline{m}$
M	number of states in airloads theory
N	number of inflow states
$\overline{p}$	location of maximum camber for NACA four-digit airfoils, *tenths chord*
p	$0.1\overline{p}$
ΔP	pressure drop across airfoil, N/m^2
t	time, *sec*
T_n	Chebychev polynomials of the first kind
u_0	velocity component in the x direction, m/s
v	total induced velocity, m/s
v_0	velocity component in the y direction, m/s
v_1	veloctiy gradient, m/s
$\overline{v}$	induced flow due to bound circulation, m/s
w_n	components of total velocity field, m/s
x	Cartesian coordinate
y	Cartesian coordinate
α	airfoil angle of attack, rad
α_{0L}	angle of zero lift, rad
α_{shift}	horizontal shift in stall angle, rad
β	trailing edge flap deflection, rad
Γ	total bound circulation, m^2/s
$\overline{\Gamma}_n$	loss in circulation due to dynamic stall of nth generalized load, m^2/s
γ	circulation per unit length, m/s
γ_b	bound circulation, m/s
γ_n	components of velocity due to bound circulation, m/s
γ_w	wake circulation, m/s
θ	effective angle of atttack, rad
λ	induced flow from trailed circulation, m/s
ξ	dummy variable of integration
ρ	density of air, kg/m^3
τ	non-dimensional time $u_0 t/b$

τ_n	expansion coefficients for $\Delta P/2$, m^2/s^2
φ	Glauert variable, rad
φ_m	Glauert variable at the flap hinge location d, rad
ϕ	phase lag between pitch and flap motion, deg
ω	frequency, rad/s
$(\dot{})$	$\partial(\,)/\partial t$
$(\,^*\,)$	$\partial(\,)/\partial \tau$

1 Introduction

Helicopter rotor blades frequently encounter dynamic stall during normal flight conditions, limiting the applicability of classical thin-airfoil theory at large angles of attack. Also, it is evident that because of the largely different conditions on the advancing and retreating sides of the rotor, future rotorcraft will employ dynamically morphing airfoils (trailing edge flaps, dynamic camber, dynamic droop, etc.) to improve efficiency and lift, while reducing noise. Dynamic stall remains a largely unresolved problem in aerodynamics, and is typically handled by semi-empirical models, based on wind tunnel results. An approach developed by ONERA and extended by Peters and Rudy describes dynamic stall behavior with a set of ordinary differential equations. This paper will demonstrate that this stall model may be integrated with a state-space airloads theory, providing a unified model to handle unsteady airloads for morphing airfoils in dynamic stall. Experimental correlations to combined pitch-flap oscillation test data are presented, which support the validity of this approach.

2 A Unified Airloads Model

A unified airloads model must allow for arbitrary airfoil motion, unsteady free-stream, morphing airfoil shape, and dynamic stall. There are three key elements of the unified model: the Peters state-space airloads theory, the 2D dynamic inflow model, and the modified ONERA dynamic stall model. This section summarizes the derivation and development of each of these components of the theory.

2.1 Peters State-Space Airloads Theory

The derivation of the Peters State-Space Airloads theory from first principles is presented, following the procedure of Ref. 1. Consider a thin airfoil of arbitrary shape moving through a mass of still air, as shown in Fig. 1. The coordinate system is centered at the mid-chord, so that $-b \leq x \leq +b$. The coordinate system is moving with some arbitrary motion, described by horizontal velocity u_0, vertical velocity v_0, and velocity gradient v_1. The deformations of the airfoil within the reference frame are considered small, such that $h << b$, $\partial h/\partial x << 1$, and $\partial h/\partial t << u_0$. Furthermore, the trailing vorticity is assumed to be shed along the x-axis. The frame is allowed to have arbitrarily large motion.

As is the case for classical thin airfoil theory, the system is constrained by the non-penetration boundary condition at the airfoil surface. The non-penetration boundary condition can be expressed as:

$$w = \overline{v} + \lambda = u_0 \frac{\partial h}{\partial x} + \frac{\partial h}{\partial t} + v_0 + v_1 \frac{x}{b} \tag{1}$$

The first two terms on the right-hand side of Eq. 1 are the result of the shape of the airfoil mean-line. It is apparent that the theory captures both static and dynamic shape changes, making the theory applicable to dynamically morphing airfoils. From the Biot-Savart law, $\overline{v}$ may be expressed in terms of the bound circulation per unit length γ_b over the interval $-b \leq x \leq +b$, corresponding to the airfoil:

$$\overline{v} = -\frac{1}{2\pi} \int_{-b}^{+b} \frac{\gamma_b(\xi, t)}{x - \xi} d\xi \tag{2}$$

Similarly, the induced flow from trailed circulation may be expressed in terms of the wake vorticity:

$$\lambda = -\frac{1}{2\pi}\int_{+b}^{\infty} \frac{\gamma_w(\xi,t)}{x-\xi}\, d\xi \tag{3}$$

The vorticity equation gives the loading due to the circulation as:

$$\Delta P = \rho u_0 \gamma_b + \rho \int_{-b}^{x} \frac{\partial \gamma_b}{\partial t}\, d\xi \;\; (-b \le x \le +b) \tag{4}$$

The spatial gradient of the induced flow due to shed wake is related to the temporal gradient of the induced flow by the relation:

$$\frac{\partial \lambda}{\partial t} + u_0 \frac{\partial \lambda}{\partial x} = \frac{1}{2\pi}\frac{d\Gamma/dt}{b-x} \tag{5}$$

Equations (1-5) define the airloads theory, which must be expressed in terms of the generalized loads, frame motions, and blade deformations. To do this, all of the variables are expressed as expansions with respect to the Glauert variable, φ. The change of variable is given by:

$$x = b\ \mathrm{Cos}\ \varphi \;\; (-b \le x \le +b,\;\; 0 \le \varphi \le \pi) \tag{6}$$

After substitution, the expansions are as follows:

$$\gamma_b = 2\left[\frac{+\gamma_s}{\mathrm{Sin}\ \varphi} - \frac{\gamma_0\ \mathrm{Cos}\ \varphi}{\mathrm{Sin}\ \varphi} + \sum_{n=1}^{\infty} \gamma_n\ \mathrm{Sin}(n\varphi)\right] \tag{7}$$

$$\Delta P = 2\rho\left[\frac{+\tau_s}{\mathrm{Sin}\ \varphi} - \frac{\tau_0\ \mathrm{Cos}\ \varphi}{\mathrm{Sin}\ \varphi} + \sum_{n=1}^{\infty} \tau_n\ \mathrm{Sin}(n\varphi)\right] \tag{8}$$

Similarly, the blade deformation and induced flow may be expressed in terms of the Glauert variable.

$$\lambda = \sum_{n=0}^{\infty} \lambda_n\ \mathrm{Cos}\ (n\varphi) \tag{9}$$

$$h(x) = \sum_{n=0}^{\infty} h_n\ \mathrm{Cos}\ (n\varphi) \tag{10}$$

The $\mathrm{Cos}(n\varphi)$ terms in Eqs. (9) and (10) are equivalent to the Chebychev polynomials, $T_n(x/b)$. These mode shapes are quite intuitive, as illustrated in Fig. 2. The first three modes correspond to plunge, pitch and camber respectively. One can simplify the pressure expression in Eq. 8, by means of the Kutta condition:

$$\tau_s = f\tau_0 \tag{11}$$

The reversed-flow parameter f is needed to enforce the condition that $\Delta P = 0$ at the trailing edge. When the flow reverses, the leading and trailing edges are interchanged, so the sign of f must also change. In general, there are various choices of f in accounting for reversed flow. For instance, if $f \equiv \mathrm{Sgn}(u_0)$, the loads will change sign instantaneously (full reversed flow). For a smoother transition to the reversed flow region, one could define $f \equiv \mathrm{Cos}\ \alpha$ (soft reversed flow). Such an assumption must be made for helicopters in forward flight, where reversed flow exists. However, since the current research deals with steady 2D flow, there is no reversed flow, and the value of f will typically be unity.

The airloads can be expressed in terms both of the airfoil motions w_n and of the uniform component of induced flow, λ_0, by expansion of the vorticity equation, Eq. (4):

$$\begin{aligned} u_0(w_0 - \lambda_0) &= \tau_0 \\ b(\dot{w}_0 - 1/2\dot{w}_2) + u_0 w_1 &= \tau_1 \\ \frac{b}{2n}(\dot{w}_{n-1} - \dot{w}_{n+1}) + u_0 w_n &= \tau_n \quad n > 2 \end{aligned} \tag{12}$$

Equation (12) is expressed in terms of the Glauert loadings. In order to find the generalized loadings, we express w_n in terms of the frame motions (u_0, v_0, and v_1) and the blade deformation $h(x,t)$ as follows:

$$\begin{aligned} w_0 &= v_0 + \dot{h}_0 + u_0 \sum_{n=1,3,5}^{\infty} n h_n/b \\ w_1 &= v_1 + \dot{h}_1 + 2u_0 \sum_{n=2,4,6}^{\infty} n h_n/b \\ w_m &= \dot{h}_m + 2u_0 \sum_{n=m+1,m+3}^{\infty} n h_n/b \quad m \geq 2 \end{aligned} \tag{13}$$

The generalized loads are determined by substitution into the following relation:

$$L_n = \int_{-b}^{+b} \Delta P \ \mathrm{Cos}(n\varphi)\ dx = -\int_0^{\pi} b\Delta P \ \mathrm{Cos}(n\varphi)\ \mathrm{Sin}\ \varphi\ d\varphi \tag{14}$$

The final result for the generalized loads is:

$$\begin{aligned} L_0 &= -2\pi\rho b f u_0(w_0 - \lambda_0) - \pi\rho b u_0 w_1 - \pi\rho b^2(\dot{w}_0 - 1/2\dot{w}_2) \\ L_1 &= \pi\rho b u_0(w_0 - \lambda_0) - 1/2\pi\rho b u_0 w_2 - 1/8\pi\rho b^2(\dot{w}_1 - \dot{w}_3) \\ L_2 &= 1/2\pi\rho b u_0(w_1 - w_3) + 1/2\pi\rho b^2(\dot{w}_0 - 1/2\dot{w}_2) - 1/12\pi\rho b^2(\dot{w}_2 - \dot{w}_4) \\ L_n &= 1/2\pi\rho b u_0(w_{n-1} - w_{n+1}) + \frac{1}{4(n-1)}\pi\rho b^2(\dot{w}_{n-2} - \dot{w}_n) \\ &\quad - \frac{1}{4(n+1)}\pi\rho b^2(\dot{w}_n - \dot{w}_{n+2}) \quad n \geq 3 \end{aligned} \tag{15}$$

Similarly, the total bound circulation is found to be:

$$\Gamma = 2\pi b\left[f(w_0 - \lambda_0) + 1/2 w_1 - 1/2\lambda_1\right] \tag{16}$$

Equations (15-16) form the basis of the airloads theory. They can be written more compactly in matrix form as follows:

$$\begin{aligned} \frac{1}{2\pi\rho}\mathbf{L}_n = &-b^2\,\mathbf{M}\left(\ddot{\mathbf{h}}_n + \dot{\mathbf{v}}_n\right) - b u_0\,\mathbf{C}\left(\dot{\mathbf{h}}_n + \mathbf{v}_n - \lambda_0\right) - {u_0}^2\,\mathbf{K}\,\mathbf{h}_n \\ &- b\,\mathbf{G}\left(\dot{u}_0\,\mathbf{h}_n - u_0\,\mathbf{v}_n + u_0\,\lambda_0\right) \end{aligned} \tag{17}$$

$$\frac{1}{2\pi}\mathbf{\Gamma} = b\,\mathbf{1}^T\left(\mathbf{C} - \mathbf{G}\right)\left(\dot{\mathbf{h}}_n + \mathbf{v}_n - \lambda_1\right) + u_0\,\mathbf{1}^T\,\mathbf{K}\,\mathbf{h}_n \tag{18}$$

The definitions of the various matrices and vectors is given in the appendix.

2.2 2D Dynamic Inflow Model

As described above, the state-space airloads theory requires some knowledge of the induced flow, λ. This is completely uncoupled from the airloads equations, so any suitable inflow model could be used. For a helicopter in forward flight, the Peters-He 3D Dynamic Inflow model could be used (Ref. 2). However, for consideration of airloads in two dimensions, a two-dimensional dynamic inflow model is used. Reference 3 utilizes a potential function expansion of the induced wake velocity, expressed in functional form. Application of the non-penetration boundary condition gives the resulting differential equation for the generalized inflow states:

$$\begin{aligned} b\dot{\lambda}_0 - b/2\ \dot{\lambda}_2 + u_0\lambda_1 &= 2\dot{\Gamma} \\ (b/2n)(\dot{\lambda}_{n-1} - \dot{\lambda}_{n+1}) + u_0\lambda_n &= (2/n)\dot{\Gamma} \quad n = 2,3,4,\ldots \end{aligned} \tag{19}$$

This provides a differential equation for all of the generalized inflow components $\lambda_1, \lambda_2, \ldots$; however, one additional equation is needed in order to close the loop. The only component of inflow needed in the airloads calculation is λ_0, which must be defined in terms of the other components. Reference 3 shows that λ_0 may be approximated by the relation

$$\lambda_0 \approx \frac{1}{2} \sum_{n=1}^{N} b_n \, \lambda_n \tag{20}$$

Substituting this relation into the error functional, Peters, *et al*, show that the error in λ_n is given by

$$error = \int_0^1 \left[1 - \sum b_n e^{-n\eta}\right]^2 \frac{1}{\text{Sinh } \eta} \, d\eta \tag{21}$$

From Eq. (21), the quantity in brackets must vanish at $\eta = 0$ in order to cancel the singularity. This leads to the constraint that $\sum b_n = 1$. While there are several possible choices for defining the b_n which satisfy these constraints, the augmented least squares approach is shown to produce the best approximation to classical aerodynamic theories, given by Eq. (22).

$$\begin{aligned} b_n &= (-1)^{n-1} \frac{(N+n)!}{(N-n)!} \frac{1}{(n!)^2} \quad n = 1, 2, \ldots, N-1 \\ b_N &= (-1)^{(N+1)} \end{aligned} \tag{22}$$

Equations (19, 20 and 22) define the inflow model used in the current airloads theory, however they need to be put into matrix form for implementation. The matrix form of Eq. (19) is given by:

$$b \, \mathbf{A} \, \dot{\lambda} + u_0 \, \lambda = \mathbf{c}(\dot{w}_0 + 1/2 \, \dot{w}_1) b \tag{23}$$

where the matrices and vectors are defined in the appendix. By using Eq. (13), the velocity vector $\mathbf{w}$ may be expanded in terms of the blade motions and free stream velocities, resulting in the expression:

$$\dot{\lambda} = \mathbf{A}^{-1} \left\{ \mathbf{c} \left[\mathbf{e}^T \left(\dot{\mathbf{v}}_n + \ddot{\mathbf{h}}_n \right) + \frac{u_0}{b} \, \mathbf{f}^T \, \dot{\mathbf{h}}_n \right] - \frac{u_0}{b} \, \lambda \right\} \tag{24}$$

2.3 ONERA Dynamic Stall Model

In the early 1980's, the French aerospace research institute ONERA sought to develop a differential equation model of dynamic stall. This was motivated largely by rotorcraft in forward flight, where there is always a portion of the rotor on the retreating side that undergoes dynamic stall. As the rotor rotates around the azimuth, the blade section oscillates in and out of the stall regime, resulting in hysteresis of the lift and moment curves.

Figure 3 illustrates the phenomenon of stall in the static lift curve. Up to the static stall angle α_{ss}, the airfoil behaves according to linear, thin-airfoil theory. Beyond that point, the airfoil begins to stall, and there is a discrepancy between the projection of the linear lift and the actual lift. That difference is the static loss of lift, denoted ΔC_L. The static loss of lift acts as the forcing function to drive the differential equation for dynamic stall. Similarly, a static loss ΔC_q may be defined for any of the airloads C_q of interest.

It is still not possible to analyze dynamic stall fully in a purely theoretical way, accounting for all of the physics. However, Ref. 4 notes that physical systems may be modeled as transfer functions, with inputs and outputs. These transfer functions and their associated differential equations may be written down based upon experimental observation, even if the underlying physics are not completely defined. It is along this line that the ONERA dynamic stall was developed, and extensive experimental correlations were done by Refs. 4, 5, 6 and others. ONERA noted that, in the linear regime (below α_{ss}), the behavior of the airloads is well described by a first-order transfer function. In the stalled regime, the airloads have a time delay and overshoot due to the passing of shed vorticity. In order to allow for this phenomenon, a second-order transfer function is used. Thus the form of the original ONERA model is given by Eqs. (25) - (27), where

the parameters λ, a, s, δ, η, ω, and e are determined by parameter identification. Implicit in the ONERA derivation is a steady free-stream velocity.

$$C_L = C_{L1} + C_{L2} \tag{25}$$

$$\overset{*}{C}_{L1} + \lambda C_{L1} = \lambda a\theta + (\lambda s + \delta)\overset{*}{\theta} + s\overset{**}{\theta} \tag{26}$$

$$\overset{**}{C}_{L2} + \eta\overset{*}{C}_{L2} + \omega^2 C_{L2} = -\omega^2\left[\Delta C_L + e\,\frac{\partial \Delta C_L}{\partial \theta}\,\overset{*}{\theta}\right] \tag{27}$$

Equation (26) in the ONERA model is for calculating the linear airloads, and Eq. (27) is for calculating the decrement in the airloads due to dynamic stall. The results are combined by superposition to determine the total airloads. ONERA found that correlation could be improved by introducing a pure time delay for the onset of stall, following the work of Beddoes (Ref. 7). However, this pure time delay introduces new non-linearities into the system, as well as an infinite number of states.

References 8 and 9 note that the model may be written equivalently in terms of lift coefficient, circulation per unit length, or normalized lift per unit length, Eqs. (26), (28) and (29).

$$\overset{*}{\overline{\Gamma}}_1 + \lambda\overline{\Gamma}_1 = \lambda aU\theta + (\lambda s + \delta)U\overset{*}{\theta} + sU\overset{**}{\theta} \tag{28}$$

$$\overset{*}{\overline{L}}_1 + \lambda\overline{L}_1 = \lambda aU^2\theta + (\lambda s + \delta)U^2\overset{*}{\theta} + sU^2\overset{**}{\theta} \tag{29}$$

For a steady free-stream, these three forms are exactly equivalent, so all three may be considered the original ONERA model. If an unsteady free-stream is considered, the three forms are not the same, due to $\overset{*}{U}$ terms that arise from the transformation of one form to the other. Using the flap response of a simplified rotor, Peters and Rudy showed that the original ONERA formulation, using lift coefficient, has an instability that can occur at large angles of attack. They determined that the formulation of the model that is best behaved and agrees most closely with experimental data is Eq. (28), in terms of circulation. This is intuitive, as dynamic stall is the result of lost circulation as vortices are shed at the leading edge. In addition, they showed that angle of attack due to plunge must be treated independently from that due to pitch. Third, they showed that apparent mass lift should not be treated by the same transfer function that is used for circulatory lift. The modifications extend the model into the rotorcraft regime, allowing unsteady free-stream, large angles of attack, and plunge. The model also recovers both Greenberg and Theodorsen theories as special cases. ONERA adopted the changes proposed by Peters and Rudy (Ref. 6).

The final form of the modified ONERA model given by Ref. 8 for a rotating system, divided into x and y components, and neglecting higher order terms, is

$$\overline{k}\,\overset{+}{\overline{\Gamma}}_1 + \lambda\overline{\Gamma}_1 = \lambda aU_y + \delta\overline{b}\,\overset{+}{\epsilon} \tag{30}$$

$$\overline{k}^2\overset{++}{\overline{\Gamma}}_2 + \overline{k}\eta\overset{+}{\overline{\Gamma}}_2 + \omega^2\overline{\Gamma}_2 = -\omega^2\left[U_x\Delta C_L + e\overline{k}\left(\overset{+}{U}_x\Delta C_L + \frac{\partial \Delta C_L}{\partial \theta}\,\overset{+}{U}_y\right)\right] \tag{31}$$

where $\overset{+}{(\,)}$ implies differentiation with respect to nondimensional time based on the average u_0, $\overline{k}$ is b/r and ϵ is the rotation of the airfoil with respect to the air mass.

In general, these differential equations may have non-constant coefficients. The variables that lead to non-linearities must be included in the coefficients. Thus an assumption is made that the coefficients change sufficiently slowly to allow the system to be linearized for small perturbations about a mean angle of attack. By observing the local behavior of the system through a range of mean angles, the behavior of the coefficients may be determined by a curve fit. A limitation of this approach is that the passage of a shed vortex occurs rapidly, testing the limits of this assumption. Nonetheless, experience has shown that good results can be acheived with the model if the stall parameters are identified carefully (Ref. 6).

2.4 The Unified Model

To illustrate how the theories above are integrated into a unified model, consider the case of an airfoil with a trailing-edge flap. A flap deflection results in an effective change in airfoil shape. In theory, to apply the ONERA dynamic stall model, static data must be known for each combination of flap deflection and angle of attack, or alternatively each combination of the generalized velocities w_0, w_1, ... Recall that the Peters state-space airloads model is hierarchical, expanded in terms of Chebyschev polynomials. Just enough states are added to be able to capture the physical behavior. We propose that dynamic stall may be handled in the same way.

Published data on cambered NACA xx12 airfoils provide a static stall database in terms of w_0, w_1, and w_2. It is assumed that data collected at low Mach number may be scaled up to higher Mach numbers, as demonstrated by Ref. 10. Further it is assumed that each generalized load has the identical stall parameters (ω, η, and e), as these should be a general property of the flow. Note that this assumption is not required. A more refined model could be be obtained by identifying stall parameters for each individual load, but that will be left to future researchers. The main goal of this research is to show that, to first order, one can determine any airload on any type of morphing airfoil by using a single set of static stall data and a single set of stall parameters for a given airfoil family.

The linear airloads are calculated by the Peters state-space airloads theory with dynamic inflow, Eqs. (17) and (23). Then, the total load including dynamic stall is calculated by Eqs. (32) and (33).

$$\frac{b^2}{{u_0}^2}\ddot{\overline{\Gamma}}_n + \eta\frac{b}{u_0}\dot{\overline{\Gamma}}_n + \omega^2\overline{\Gamma}_n = -bu_0\omega^2\left[\Delta C_n + e\,\frac{\partial \Delta C_n}{\partial\theta}\,\dot{\theta}\frac{b}{u_0}\right] \tag{32}$$

$$L_n = L_{n(linear)} + \rho u_0 \overline{\Gamma}_n \tag{33}$$

Finally, the lift and moment coefficients are calculated from the generalized loads. The result is a hierarchical unsteady airloads theory for morphing airfoils in dynamic stall.

3 Static Airfoil Section Characteristics

The dynamic stall model is forced by the static stall, which is a function of airfoil shape. For fixed airfoils, section characteristics may be obtained from published airfoil tables, wind tunnel testing, boundary layer analysis codes, etc. However, morphing airfoils have static section characteristics that change as the airfoil shape changes. There are currently no tables available for morphing airfoils, and only limited wind tunnel test data exist. Reference 11 uses a table lookup with data generated by the XFOIL boundary-layer analysis software. The current research will use a different approach, generalizing published airfoil tables to estimate the static section characteristics of an arbitrary airfoil shape based on the first three generalized velocity components.

A static stall data base is built from published data on eighteen NACA four-digit airfoils (Ref. 12). The data were collected in the NACA variable-density wind tunnel under uniform flow conditions, with 12% thickness and camber ranging from 0 to 6%. The point of maximum camber ranges from 0.2 to 0.7 chord. NACA four-digit airfoils are denoted NACA$\overline{m}\,\overline{p}\,x\,y$. The first digit represents the percent camber, the second digit is the chordwise position of the maximum ordinate, and the last two digits are the maximum airfoil thickness.

To quantify the effect of airfoil camber, consider an airfoil in a steady horizontal free stream. The non-penetration boundary condition is given by:

$$w = u_0\,\partial h/\partial x + \partial h/\partial t + v_0 + v_1\,x/b \tag{34}$$

For static 2D testing, the only non-zero velocity component is given by the spatial gradient term $u_0\,\partial h/\partial x$. This represents the portion of the velocity due to the camber of the airfoil. If the spatial gradient is zero, one recovers the flat-plate airfoil results. The first three velocity components may be written explicitly by a

Glauert expansion, as given by Eq. (36-38), where $q = b(2p-1)$.

$$w = u_0\, \partial h/\partial x = \sum_{n=0}^{\infty} w_n \mathrm{Cos}\ n\varphi \tag{35}$$

$$w_0 = \frac{4qmu_0}{(b^2-q^2)^2}\left[\frac{4}{\pi}\left(b^2\sqrt{1-\frac{q^2}{b^2}} + bq\,\mathrm{ArcSin}\ \frac{q}{b}\right) - \left(b^2+q^2\right)\right] \tag{36}$$

$$w_1 = \frac{4bmu_0}{(b^2-q^2)^2}\left[\left(b^2+q^2\right) - \frac{4}{\pi}\left(bq\,\mathrm{ArcSin}\ \frac{q}{b} + q^2\sqrt{1-\frac{q^2}{b^2}}\right)\right] \tag{37}$$

$$w_2 = \frac{32mu_0}{3\pi b^4}\frac{q}{b^2-q^2}\sqrt{1-\frac{q^2}{b^2}} \tag{38}$$

A summary of the data set used is shown in Fig. 4. It is apparent from the figures that all of the airfoils show the same general trends in the behavior of C_L and C_M during stall, however the angle at which stall occurs varies as a function of camber. Furthermore, the curves are shifted due to the fact that cambered airfoils produce lift even at zero angle of attack. Clearly some consolidation of the curves is necessary in order to produce a parametric representation of the lift and moment curves. The theoretical angle of zero lift is calculated by finding the point at which $w_0 + \frac{1}{2}\, w_1 = 0$. Table 1. shows the computed angles of zero lift, along with a comparison to the observed results from the published data for the eighteen airfoils being considered. The predicted and actual angles agree relatively well, but begin to show less agreement at higher values of camber.

Table 1: Angle of zero lift for NACA xx12 airfoils

Airfoil	w_0	w_1	Predicted α_{0L} (°)	Actual α_{0L} (°)
0012	0.000	0.000	-0.00	-0.0
2212	-0.018	0.098	-1.80	-1.8
2312	-0.010	0.087	-1.92	-1.9
2412	-0.005	0.082	-2.08	-1.8
2512	0.000	0.080	-2.29	-2.1
2612	0.005	0.082	-2.59	-2.3
4212	-0.035	0.196	-3.60	-3.4
4312	-0.020	0.173	-3.84	-3.9
4412	-0.009	0.163	-4.15	-3.9
4512	0.000	0.160	-4.58	-4.2
4612	0.009	0.163	-5.18	-4.6
4712	0.020	0.173	-6.09	-5.0
6212	-0.053	0.294	-5.40	-5.2
6312	-0.030	0.260	-5.75	-5.5
6412	-0.014	0.245	-6.23	-5.7
6512	0.000	0.240	-6.88	-6.2
6612	0.014	0.245	-7.78	-6.6
6712	0.030	0.256	-9.13	-7.0

The data are collapsed by plotting $\alpha - \alpha_{0L}$ on the abscissa, ensuring that each of the lift curves passes through the origin. The moment curve is also plotted with $\alpha - \alpha_{0L}$ on the abscissa. The moment curve has a vertical offset as well, denoted C_{M0}, due to the steady moment produced by a cambered airfoil. The theoretical moment predicted by thin airfoil theory is $-\pi/4(w_1 + w_2)$. A fit of the data shows the moment offset to be $-0.615(w_1 + w_2)$, approximately 20% less than the theoretical values. The shifted curves are shown in Fig. 5. The data are now in a form suitable for parameterization. For the purpose of the curve

fit, it is assumed that stall occurs simultaneously on the lift and moment curves. Comparison of the curves shows that this approximation is reasonable. Therefore, the section characteristics for a morphing airfoil based on the NACA xx12 family are determined by a single parameter, α_{shift}. This represents the horizontal shift of the NACA 0012 curve as a function of w_0, w_1, and w_2, given by Eq. (39).

$$\alpha_{shift} = -6.018w_0 + 0.331w_1 + 2.435w_2 \tag{39}$$

Typical results can be computed for a NACA 0012 airfoil with a trailing-edge flap hinged at 0.8 chord. A positive (flap down) deflection results in an effective increase in camber, increasing the maximum lift. A negative flap deflection results in a reduction in maximum lift and earlier onset of stall. A $\pm 6^\circ$ flap deflection results in a range of values for w_0 from -0.0314 to $+0.0314$ and w_1 from -0.0550 to $+0.0550$. These values are within the range of the data for the cambered airfoils, from which the data was generated.

4 Determination of Stall Parameters

The ONERA dynamic stall model originated from observations of the behavior of the lift and moment coefficients of an airfoil undergoing small perturbations in angle of attack. References 4 and 6 describe the development of the model. The model proposes that dynamic stall may be considered a dynamic system, modeled by a differential equation (or equivalently a transfer function). Even without a complete description of the physical phenomenon, the behavior may be modeled approximately way by a fit of the transfer function with appropriate parameters. Petot, *et al*, performed wind tunnel testing of airfoils at various mean angles of attack, undergoing 0.5° oscillations. A transfer function was fit to the experimental results, linearized about each mean angle. Finally, the results were synthesized into a non-constant coefficient second order linear differential equation, Eq. (32).

In Eq. (32), $\overline{\Gamma}_n$ represents the loss in circulation due to dynamic stall. The three parameters that determine the time delay and overshoot of the system are ω, η, and e. These parameters are not constant, but rather vary with the angle of attack. Various possibilities exist for the functional form of the parameters; however the following form was found to be the most convenient by ONERA:

$$\omega = \omega_0 + \omega_2 \, {\Delta C_L}^2 \quad \eta = \eta_0 + \eta_2 \, {\Delta C_L}^2 \quad e = e_0 + e_2 \, {\Delta C_L}^2 \tag{40}$$

The advantage of this functional form is that ΔC_L is an indicator of stall. Thus, this parameter can hold true for any combination of airfoil morphing (including camber or trailing-edge flaps). When the airfoil enters the stall regime, the right hand side of Eq. (32) is a forcing term creating a loss in circulation. The time delay and overshoot of the response, determined by ω and η, depend on the severity of stall. Once the angle of attack falls below the stall angle, then $\Delta C_L = 0$. Thus, the right-hand side of Eq. (32) vanishes; and the equation becomes a homogeneous, constant-coefficient linear ODE. The circulation loss decays back to zero and the airloads return to the linear behavior predicted by thin-airfoil theory.

In the current research, small amplitude oscillation data are not available for deriving the transfer functions with trailing-edge flaps. Instead, the stall parameters are identified using large amplitude stall data on the NACA 0012 airfoil at reduced frequencies of $k = 0.025$ and $k = 0.10$ published by NASA (Ref. 13). The dynamic stall is computed by solution of Eq. (32). ΔC_L is computed by subtracting the actual static lift curve (shown in the dashed line) from the projected linear lift. This becomes the forcing function for the differential equation. The solution is time marched for a given set of parameters at each reduced frequency. The `lsqnonlin` function in Matlab is used to identify the combination of parameters which minimizes the combined error at the two reduced frequencies in a least-squares sense. The final results of the parameter identification are given by Eq. (41).

$$\begin{aligned} \omega &= 0.2581 - 0.0264 \, {\Delta C_L}^2 \\ \eta &= 0.3861 + 0.3973 \, {\Delta C_L}^2 \\ e &= -0.0294 - 0.1607 \, {\Delta C_L}^2 \end{aligned} \tag{41}$$

It is then assumed that these same parameters will hold for all generalized loads due to all airfoil deformations.

Figure 6 shows the fit of the published data with the parameters given above (Ref. 13). The airfoil was oscillated with $\alpha = 10^\circ + 5^\circ \text{Sin } k\tau$, at reduced frequencies $k = 0.025$ and $k = 0.10$. The correlation to the experimental dynamic stall data is striking. The model slightly under-predicts the time for the stall vortex to reattach at lower reduced frequency, but certainly captures the shape and character of the curve quite well. Very little overshoot is seen at $k = 0.025$ compared to the static curve; however at $k = 0.10$, the linear character of the lift curve is extended by about 3°, resulting in an increase in C_{Lmax} of about 0.2. At the higher reduced frequency, the vortex has just reattached before beginning another cycle.

5 Combined Pitch-Flap Oscillation

The experimental data to be considered in this paper come from wind tunnel testing of a NACA 0012 airfoil with combined pitch and flap motion (Ref. 14). The airfoil is pitched about a center of rotation that is 35% chord from the leading edge, oscillating at a reduced frequency of $k = 0.021$. Simultaneously, the flap is oscillated at twice the frequency of the pitch, with reduced frequency $k = 0.042$. The center of rotation of the flap is at 80% chord from the leading edge. The experimental C_L and C_M were measured by pressure transducers on the airfoil. The equations describing the intended motion of the airfoil are given by

$$\begin{aligned} \alpha &= \alpha_0 + \overline{\alpha}\ \text{Sin}(k\tau) \\ \beta &= \beta_0 + \overline{\beta}\ \text{Sin}(2k\tau - \phi) \end{aligned} \tag{42}$$

However, due to experimental constraints, the actual α and β are more complicated curves. Through direct correspondence with the authors, the measured values of α, β, C_L, and C_M at each time step were obtained. The values of α and β were used as the input to the thin airfoil theory. They were transformed into the generalized coordinate system by expansion of the trailing edge flap geometry in a Glauert series (Ref. 1). The expansion in terms of β is

$$\begin{aligned} h_0 &= (\beta b/\pi)[\text{Sin } \varphi_m - \varphi_m \text{Cos } \varphi_m] \\ h_1 &= (\beta b/\pi)[\varphi_m - \text{Sin } \varphi_m \text{ Cos } \varphi_m] \\ h_n &= (\beta b/\pi)\left\{ \frac{1}{n+1}\text{Sin}[(n+1)\varphi_m] + \frac{1}{n-1}\text{Sin}[(n-1)\varphi_m] - \frac{2}{n}\text{Cos } \varphi_m \text{ Sin}(n\varphi_m) \right\} \end{aligned} \tag{43}$$

The above expansion allows for a matrix transformation between the user variables α and β and the generalized blade deformations h_n as follows:

$$\mathbf{h}_n = \mathbf{T} \left\{ \begin{array}{c} \alpha \\ \beta \end{array} \right\} \tag{44}$$

where $\mathbf{T}$ is defined in the appendix.

Data were recorded for various ranges of α and β and at various phase angles. There are eight cases, as shown in Table 2. Cases 1-3 never exceed the static stall angle of the airfoil, so there is no dynamic stall present. Cases 4-6 exceed the stall angle by less than 2°, so there is only moderate dynamic stall. Cases 7-8 data exceed the stall angle by as much 8°, illustrating the effects of heavy dynamic stall. The system is simulated in Matlab by simultaneously time marching Eqs. (17, 24, and 32). Time derivatives are estimated using a central difference approximation. It is assumed that the w_0, w_1, and w_2 created by the trailing-edge flap will produce the same static and dynamic-stall airfoil behavior as those same Glauert parameters did when produced by an NACA camber. This approach generalizes the methodology to arbitrary morphing dynamics. The results of the simulations are shown in Figs. 8 - 15.

Empirical correction factors f_α, f_β, f_L, and f_M are applied in order to match the static data, and then

these identical parameters are used for the unsteady correlation.

$$\mathbf{h}_n = \mathbf{T} \begin{bmatrix} f_\alpha & 0 \\ 0 & f_\beta \end{bmatrix} \begin{Bmatrix} \alpha \\ \beta \end{Bmatrix} \tag{45}$$

$$C_L = -\frac{f_L\, L_0}{\rho\, {u_0}^2\, b}, \quad C_M = \frac{f_M\, L_1 + f_L\, L_0\, a_c\, b}{2\rho\, {u_0}^2\, b^2}$$

One set of correction factors, f_α and f_β, is applied to α and β. A second set of factors, f_L and f_M, is introduced as a correction on the output. In addition, the location of the airfoil center of rotation a_c is adjusted, to obtain the proper shape of the C_M curve. We have listed five empirical correction factors: f_α, f_β, f_L, f_M, and a_c. Of these, only four are independent. For instance, if f_L and f_M are doubled while f_α and f_β are halved, the resulting C_L and C_M will be identical. For simplicity, we have defined f_L to be unity and adjusted the other factors to provide a best fit for the static data. One set of correction factors is used for the unstalled data (Cases 1-3), and a different set of correction factors is used for the stalled cases (Cases 4-8), as shown in Table 2. It is not clear why different sets are needed. However, it is encouraging that all of the stalled data are correlated reasonably well with a single set of correction factors. Also, the correction factors for the stalled data are closer to unity than the unstalled data. Each plot has a steady component, a 5 Hz component, and a 10 Hz component. Thus, there are 2x5x5=50 different components to be correlated; and only one set of four correction factors does well for the stalled data. Similarly, there are 2x3x5=30 different components correlated with one set of correction factors for the unstalled data.

6 Conclusions

A unified airloads model has been presented that includes the effects of morphing airfoil geometry and dynamic stall. The model is hierarchical, allowing the user to use just enough states to adequately model the physics, while being able to make computations efficiently in real time. It is remarkable that the theory gives a first approximation for the airloads for an airfoil undergoing arbitrary pitch and trailing-edge flap motions with parameters obtained from static data for NACA cambered airfoils and dynamic data from an NACA 0012. This verifies the soundness of this approach. Good correlation has been demonstrated for the NACA 0012 airfoil with trailing-edge flap.

Future work will include correlating the theory for other types of morphing airfoils. These may include concepts such as the variable droop leading edge (VDLE), which has been shown to significantly reduce dynamic stall due to a reduced angle of incidence at the leading edge, where stall vortices are generated (Ref. 15).

Acknowledgements

This work was funded by the U.S. Army through the Georgia Tech Center of Excellence for Rotorcraft Technology, Michael Ruthjowski technical monitor; and by NASA Ames Research Center, Grant NN A05CV28G, William Warmbrodt technical monitor.

Table 2: Empirical correction factors

Case	Dynamic stall	α	β	f_α	f_β	f_L	f_M	a_c
1-3	None	$-6°$ to $6°$	$-5°$ to $6°$	0.588	1.639	1.000	0.725	-0.304
4-6	Moderate	$-2°$ to $10°$	$-5°$ to $6°$	0.890	0.842	1.000	0.920	-0.400
7-8	Heavy	$5°$ to $16°$	$-5°$ to $6°$	0.890	0.842	1.000	0.920	-0.400

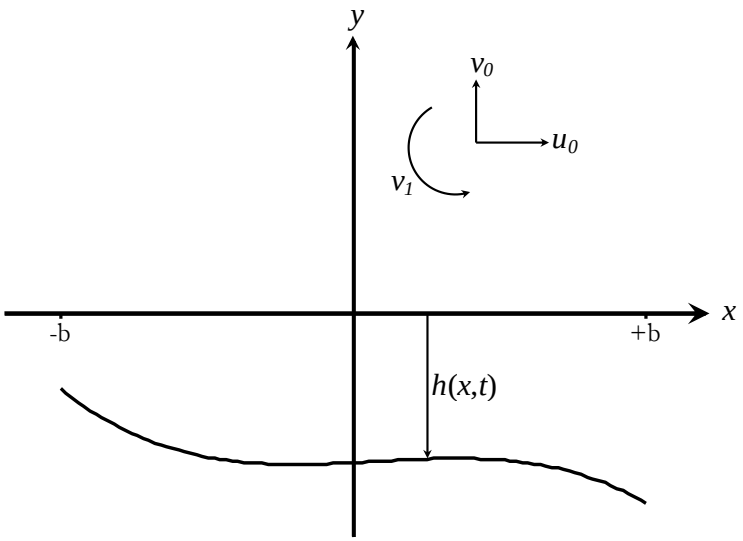

Figure 1: General airfoil coordinate system

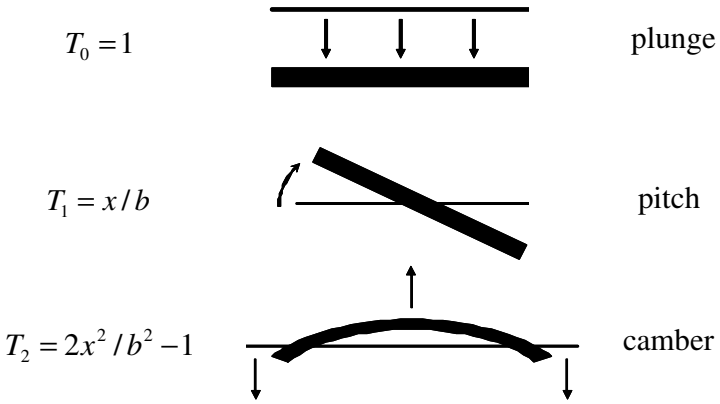

Figure 2: Physical significance of first three modes

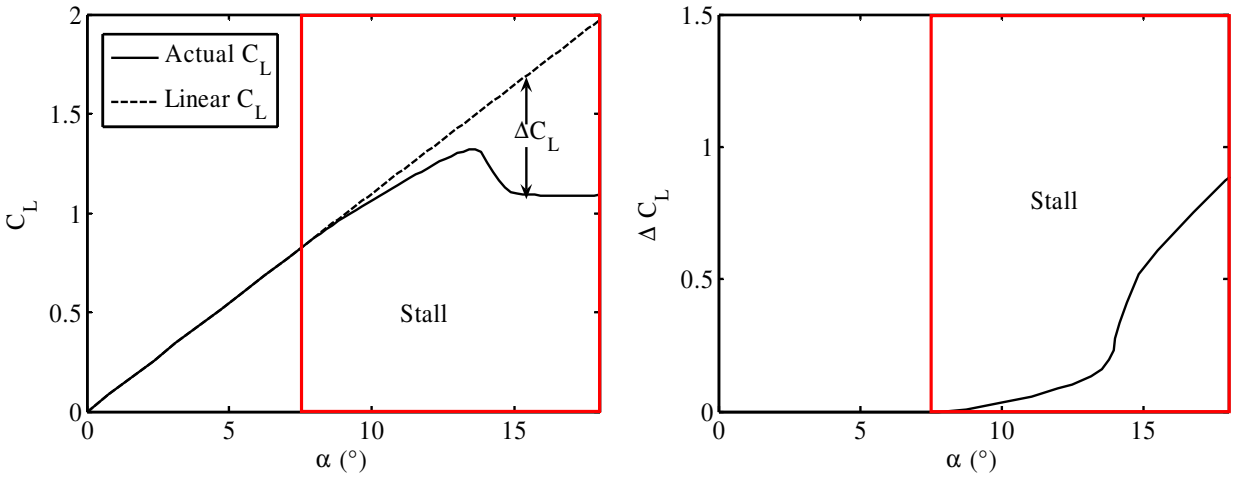

Figure 3: Illustration of static stall

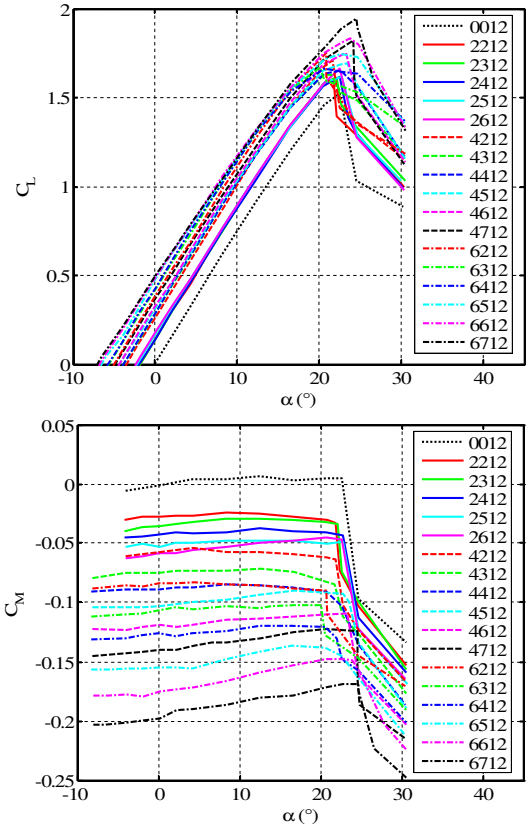

Figure 4: Section characteristics for NACA xx12 airfoils

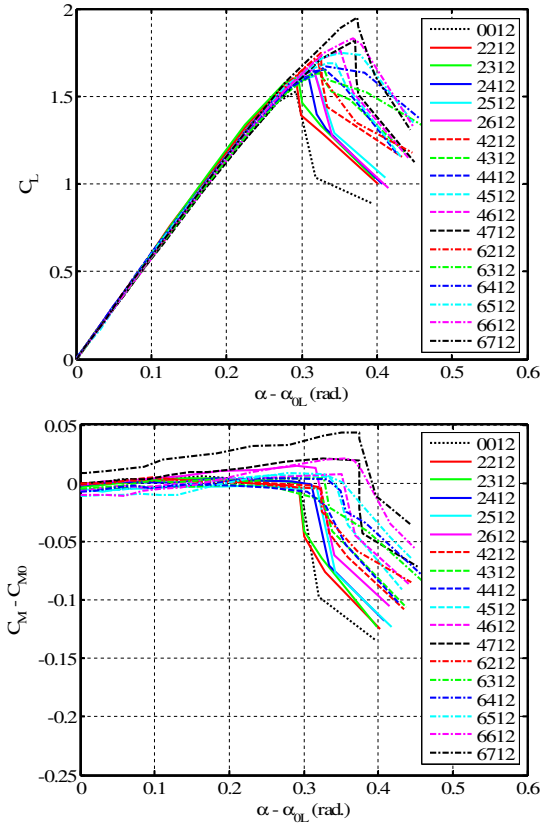

Figure 5: Collapsed section characteristics for NACA xx12 airfoils

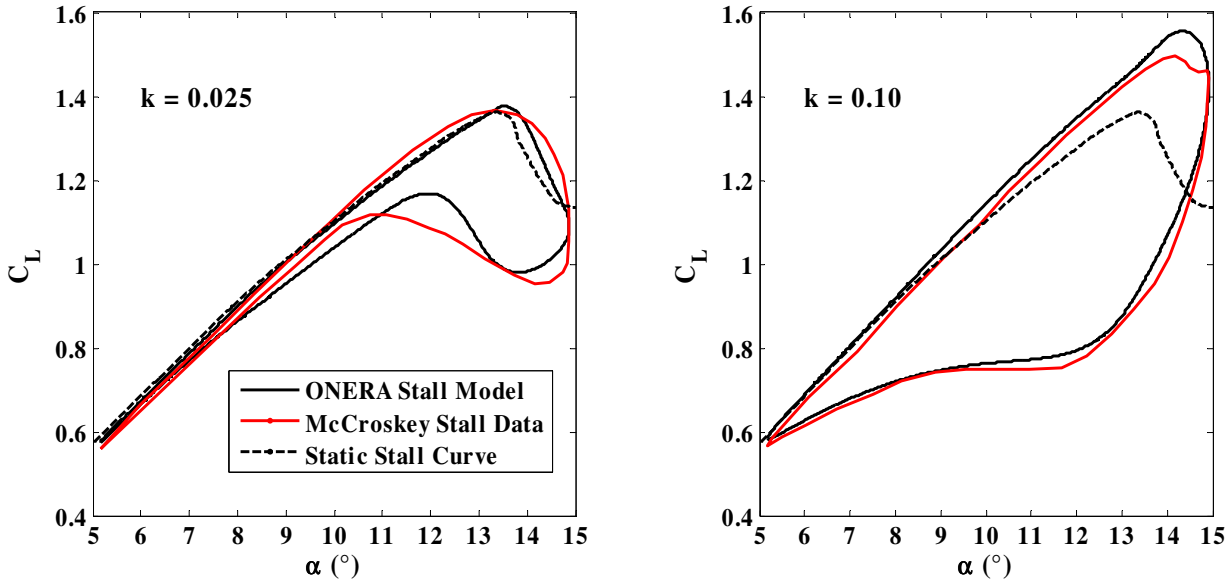

Figure 6: Least squares fit of NACA 0012 dynamic stall data

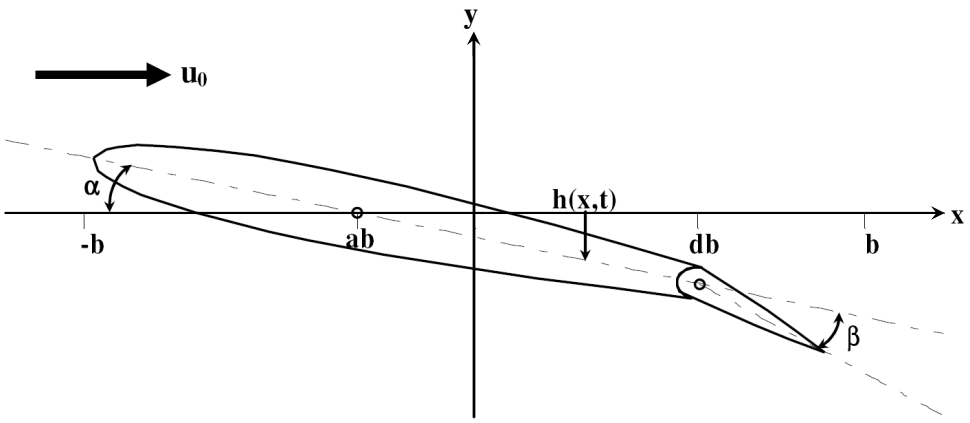

Figure 7: Experimental setup of Ref. 14

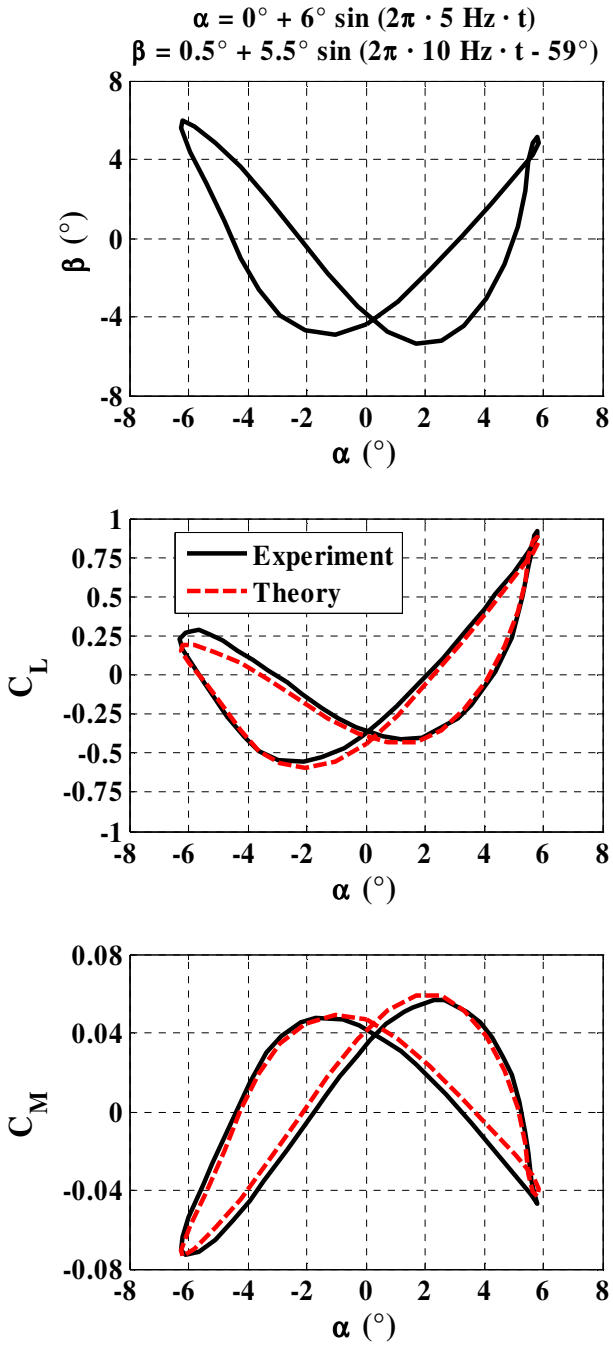

Figure 8: Case 1

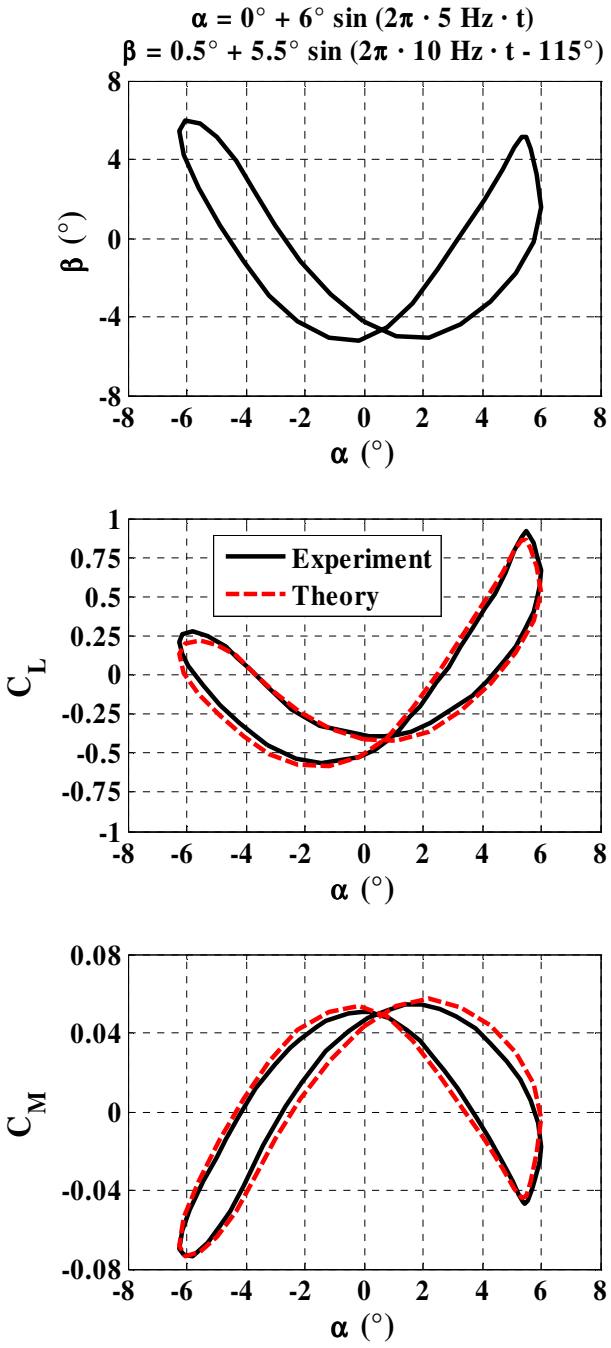

Figure 9: Case 2

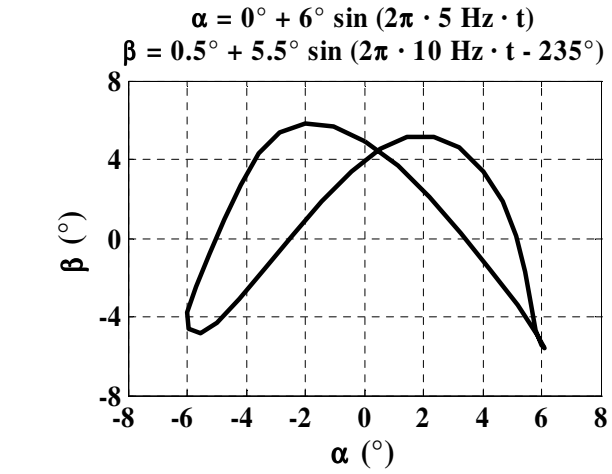

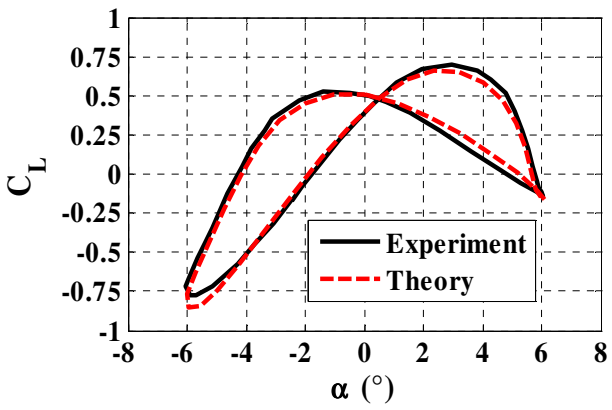

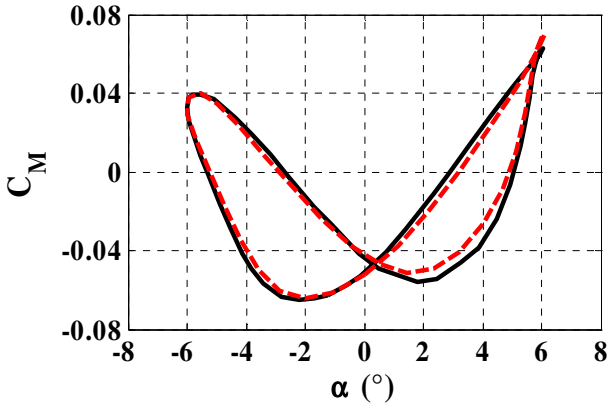

Figure 10: Case 3

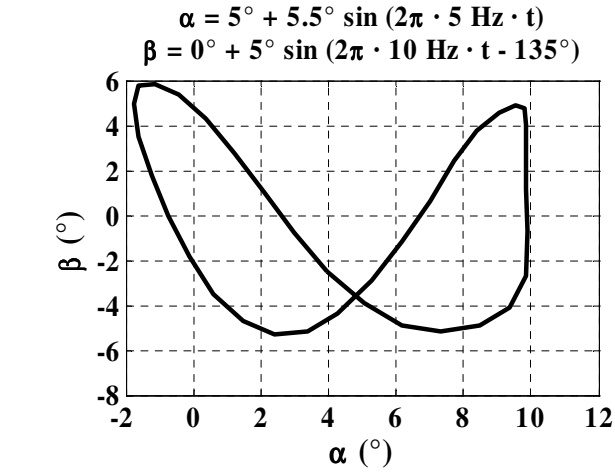

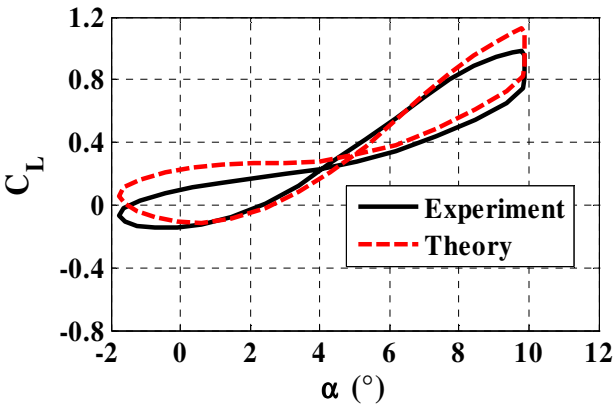

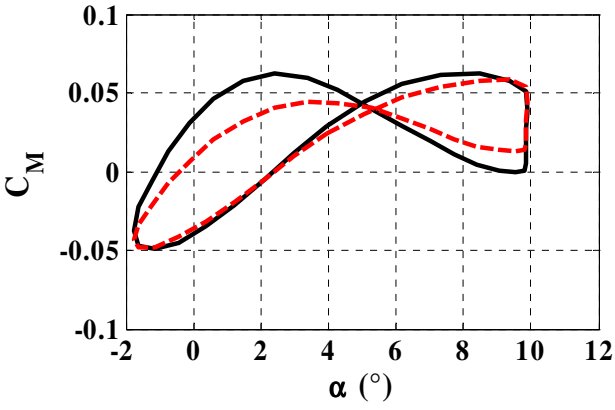

Figure 11: Case 4

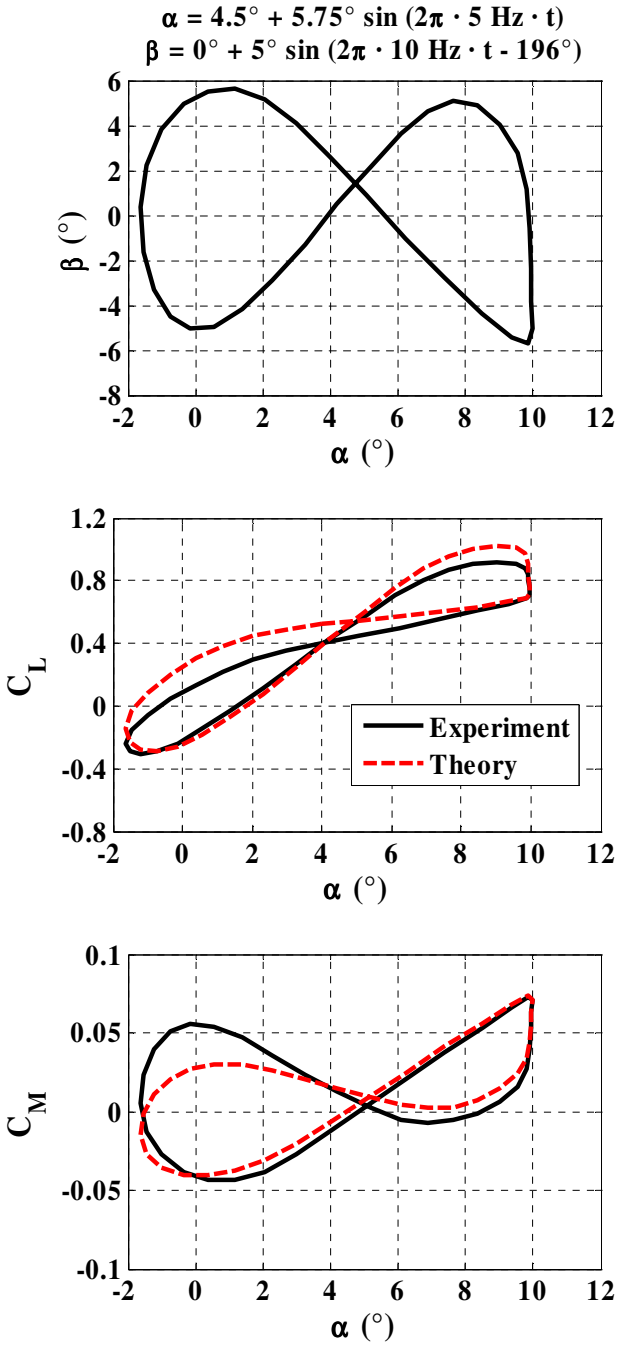

Figure 12: Case 5

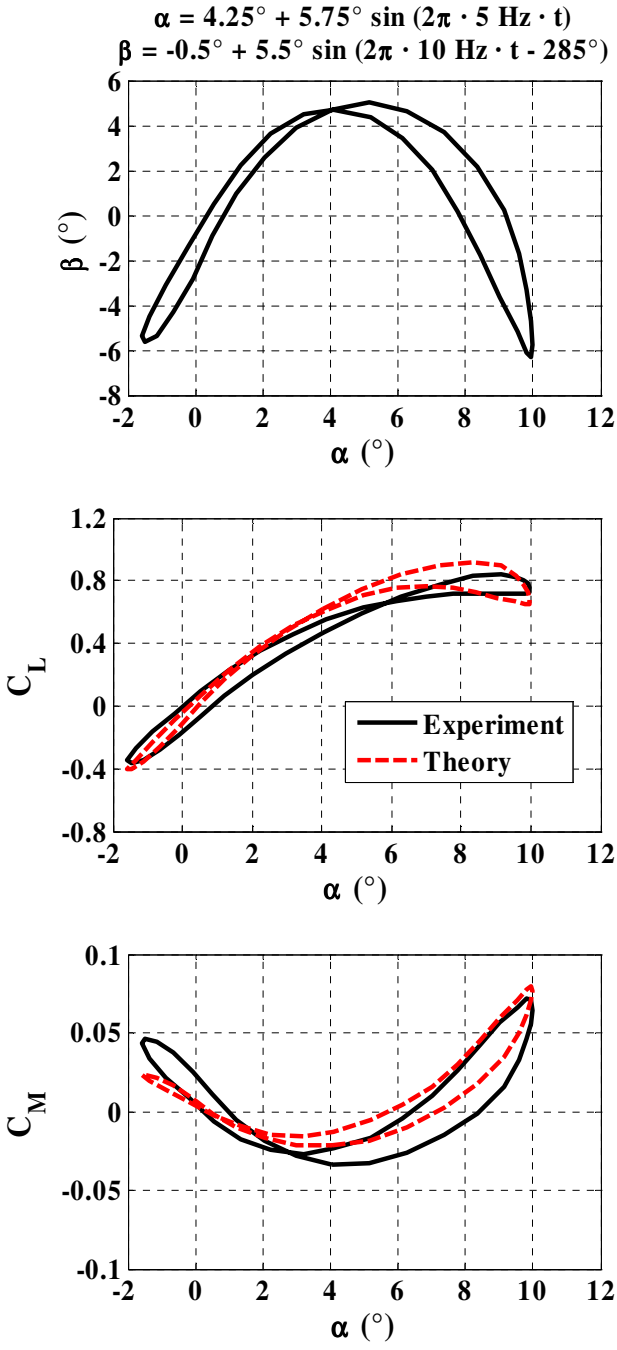

Figure 13: Case 6

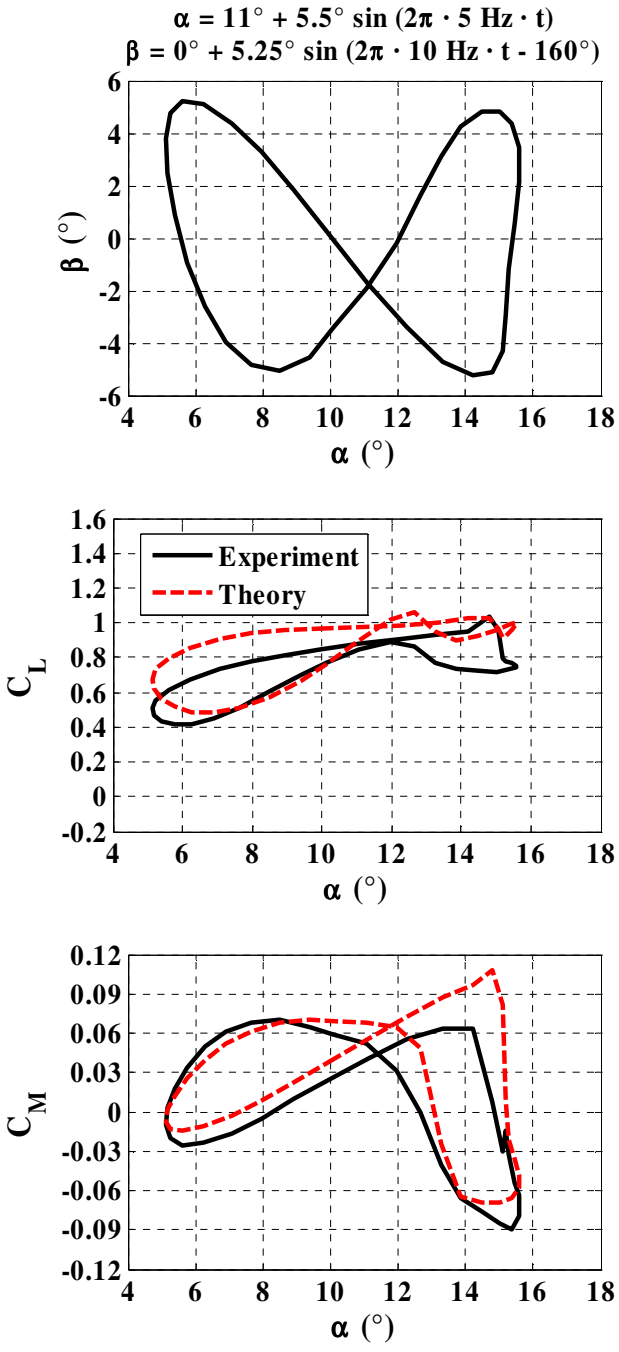

Figure 14: Case 7

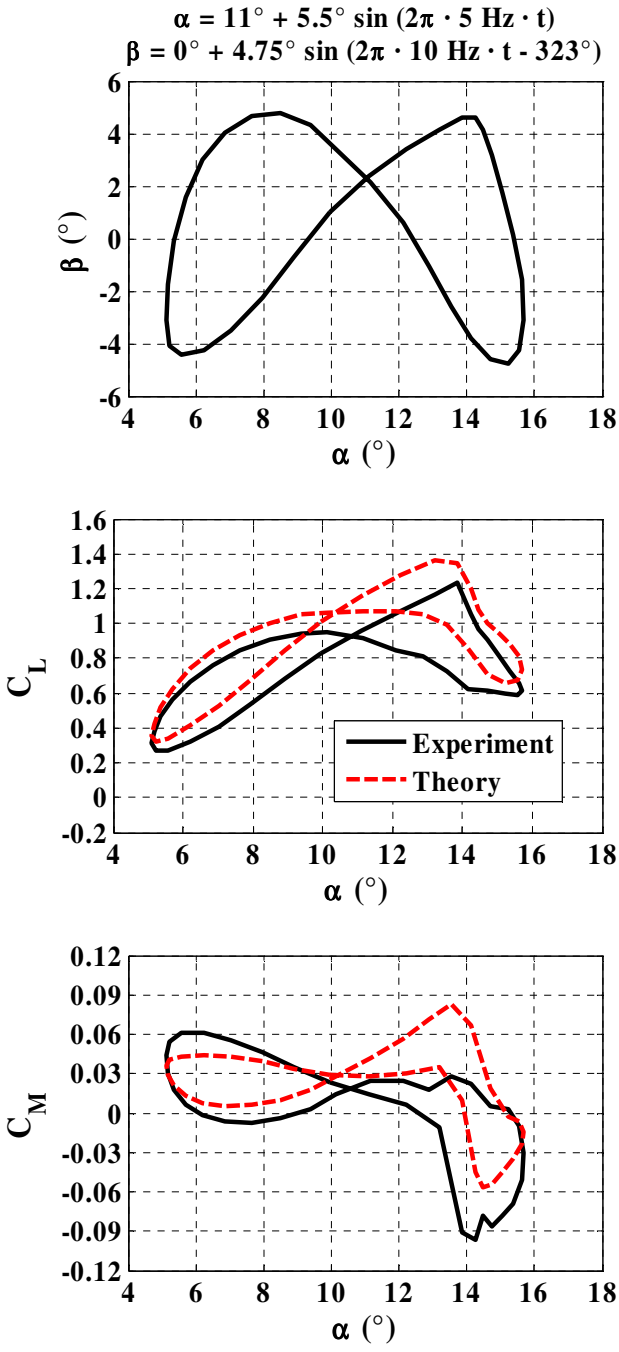

Figure 15: Case 8

Appendix

The following matrices and vectors are used in the derivation of the unified model. Note that M refers to the number of states in the Glauert expansion, resulting in $(M+1)\times(M+1)$ matrices and $(M+1)\times 1$ vectors. N refers to the number of inflow states, resulting in $N\times N$ matrices and $N\times 1$ vectors.

$\mathbf{1} = \{1 \;\; 0 \;\; 0 \;\; 0 \;\; \cdots\}^T$

$\mathbf{b} = \{b_1 \;\; b_2 \;\; b_3 \;\; \cdots \;\; b_N\}^T$ as defined by Eq. (22)

$\mathbf{c} = \left\{2 \;\; 1 \;\; \frac{2}{3} \;\; \frac{1}{2} \;\; \cdots \;\; \frac{2}{N}\right\}^T$

$\mathbf{d} = \left\{\frac{1}{2} \;\; 0 \;\; 0 \;\; 0 \;\; \cdots\right\}^T$

$\mathbf{e} = \left\{1 \;\; \frac{1}{2} \;\; 0 \;\; 0 \;\; \cdots\right\}^T$

$\mathbf{f} = \{0 \;\; 1 \;\; 2 \;\; \cdots \;\; M\}^T$

$\mathbf{h}_n = \{h_0 \;\; h_1 \;\; h_2 \;\; \cdots \;\; h_M\}^T$

$\mathbf{v}_n = \{v_0 \;\; v_1 \;\; 0 \;\; 0 \;\; \cdots\}^T$

$\dot{\mathbf{v}}_n + \ddot{\mathbf{h}}_n = \left\{\dot{v}_0 + \ddot{h_0} \;\; \dot{v}_1 + \ddot{h_1} \;\; 0 \;\; 0 \;\; \cdots\right\}^T$

$\lambda_0 = \{\lambda_0 \;\; 0 \;\; 0 \;\; 0 \;\; \cdots\}^T$

$\lambda_1 = \{\lambda_0 \;\; \lambda_1 \;\; 0 \;\; 0 \;\; \cdots\}^T$

$\mathbf{A} = \mathbf{D} + \mathbf{d}\,\mathbf{b}^T + \mathbf{c}\,\mathbf{d}^T + \frac{1}{2}\,\mathbf{c}\,\mathbf{b}^T$

$$\mathbf{C} = \begin{bmatrix} \frac{1}{2} & 0 & -\frac{1}{4} & 0 & 0 & \cdots \\ 0 & \frac{1}{16} & 0 & -\frac{1}{16} & 0 & \cdots \\ -\frac{1}{4} & 0 & \frac{1}{6} & 0 & \ddots & \ddots \\ 0 & -\frac{1}{16} & 0 & \ddots & 0 & \ddots \\ 0 & 0 & \ddots & 0 & \ddots & \ddots \\ \vdots & \vdots & \ddots & -\frac{1}{8M} & \ddots & \frac{M}{4(M^2-1)} \end{bmatrix} \quad \mathbf{D} = \begin{bmatrix} 0 & -\frac{1}{2} & 0 & 0 & \cdots & 0 \\ \frac{1}{4} & 0 & -\frac{1}{4} & 0 & \cdots & 0 \\ 0 & \frac{1}{6} & 0 & -\frac{1}{6} & \ddots & 0 \\ 0 & 0 & \frac{1}{8} & \ddots & \ddots & 0 \\ \vdots & \vdots & \ddots & \ddots & 0 & \ddots \\ 0 & 0 & 0 & 0 & \frac{1}{2N} & 0 \end{bmatrix}$$

$$\mathbf{G} = \begin{bmatrix} 0 & \frac{1}{2} & 0 & 0 & 0 & \cdots \\ 0 & 0 & \frac{1}{4} & 0 & 0 & \cdots \\ 0 & -\frac{1}{4} & 0 & \frac{1}{4} & 0 & \ddots \\ 0 & 0 & -\frac{1}{4} & 0 & \frac{1}{4} & \ddots \\ 0 & 0 & 0 & -\frac{1}{4} & 0 & \ddots \\ \vdots & \vdots & \vdots & \ddots & \ddots & \ddots \end{bmatrix} \quad \mathbf{H} = \begin{bmatrix} 0 & 0 & 0 & 0 & 0 & \cdots \\ 0 & 1/2 & 0 & 0 & 0 & \cdots \\ 0 & 0 & 2/2 & 0 & 0 & \cdots \\ 0 & 0 & 0 & 3/2 & 0 & \cdots \\ 0 & 0 & 0 & 0 & 4/2 & \cdots \\ \vdots & \vdots & \vdots & \vdots & \vdots & \ddots \end{bmatrix}$$

$$\mathbf{K} = \begin{bmatrix} 0 & f & 2 & 3f & 4 & \cdots \\ 0 & -\frac{1}{2} & 0 & 0 & 0 & \cdots \\ 0 & 0 & -\frac{2}{2} & 0 & 0 & \cdots \\ 0 & 0 & 0 & -\frac{3}{2} & 0 & \ddots \\ 0 & 0 & 0 & 0 & \ddots & \ddots \\ \vdots & \vdots & \vdots & \vdots & \ddots & -\frac{M}{2} \end{bmatrix} \quad \mathbf{M} = \begin{bmatrix} f & 1 & 0 & 0 & 0 & \cdots \\ -\frac{1}{2} & 0 & \frac{1}{2} & 0 & 0 & \cdots \\ 0 & -\frac{1}{2} & 0 & \frac{1}{2} & 0 & \cdots \\ 0 & 0 & -\frac{1}{2} & 0 & \frac{1}{2} & \ddots \\ 0 & 0 & 0 & -\frac{1}{2} & 0 & \ddots \\ \vdots & \vdots & \vdots & \ddots & \ddots & \ddots \end{bmatrix}$$

$$\mathbf{S} = \begin{bmatrix} f & 0 & 0 & 0 & 0 & \cdots \\ 0 & 0 & 0 & 0 & 0 & \cdots \\ 0 & 0 & 0 & 0 & 0 & \cdots \\ 0 & 0 & 0 & 0 & 0 & \cdots \\ 0 & 0 & 0 & 0 & 0 & \cdots \\ \vdots & \vdots & \vdots & \vdots & \vdots & \ddots \end{bmatrix}$$

$$\mathbf{T} = \begin{bmatrix} -ba & (b/\pi)[\text{Sin } \varphi_m - \varphi_m \text{Cos } \varphi_m] \\ b & (b/\pi)[\varphi_m - \text{Sin } \varphi_m \text{ Cos } \varphi_m] \\ 0 & (b/\pi)\left\{\frac{1}{n+1} \text{ Sin}[(n+1)\varphi_m] + \frac{1}{n-1} \text{ Sin}[(n-1)\varphi_m] - \frac{2}{n} \text{ Cos } \varphi_m \text{ Sin}(n\varphi_m)\right\} \\ \vdots & \vdots \end{bmatrix}$$

References

1. Peters, D. A., Hsieh, M. C., and Torrero, A. A state-space airloads theory for flexible airfoils, American Helicopter Society 62nd Annual Forum Proceedings, Phoenix, AZ, May 9-11, 2006.

2. Peters, D. A., and He, C. J. Finite state induced flow models part II: three-dimensional rotor disk, *Journal of Aircraft*, 1995, **32**, (2), pp. 323-333.

3. Peters, D. A., Karunamoorthy, S., and Cao, W. Finite state induced flow models part I: two-dimensional thin airfoil, *Journal of Aircraft*, 1995, **32**, (2), pp. 313-322.

4. Petot, D. Progress in the semi-empirical prediction of the aerodynamic forces due to large amplitude oscillations of an airfoil in attached or separated flow, Ninth European Rotorcraft Forum Proceedings, Stresa, Italy, September 1983.

5. McAlister, K., Lambert, O., and Petot, D. Application of the ONERA model of dynamic stall, NASA Technical Paper 2399, 1984.

6. Petot, D. Differential equation modeling of dynamic stall, *Rech. Aerosp.*, 1989 **5**.

7. Beddoes, T. S. A synthesis of unsteady aerodynamic effects including stall hysteresis, First European Rotorcraft Forum Proceedings, September, 1975.

8. Peters, D. A. Toward a unified lift model for use in rotor blade stability analyses, *Journal of the American Helicopter Society*, July 1985, pp. 32-42.

9. Rudy, D. J. *Comparison of Rotor Blade Flapping Response with Three Different Dynamic Stall Models*, Master of Science Thesis, Washington University, May 1983.

10. Peters, D. A., Barwey, D., and Johnson, M. Finite-state airloads modeling with compressibility and unsteady free-stream, Sixth International Workshop on Dynamics and Aeroelastic Stability Modeling of Rotorcraft Systems, November 1995.

11. Thepvongs, S., Cesnik, C. E. S., Palacios, R., and Peters, D. A. Finite-state aeroelastic modeling of rotating wings with deformable airfoils, American Helicopter Society 64th Annual Forum Proceedings, Montréal, Canada, April 29 - May 1, 2008.

12. Jacobs, E., Ward, K., and Pinkerton, R. The characteristics of 78 related airfoil sections from tests in the variable-density wind tunnel, NACA Report No. 460, 1933.

13. McCroskey, W. J., The phenomenon of dynamic stall, NASA TM 81264, March 1981.

14. Krzysiak, A. and Narkiewicz, J., Aerodynamic loads on airfoil with trailing-edge flap pitching with different frequencies, *Journal of Aircraft*, March-April 2006, **43**, (2), pp. 407-418.

15. Chandrasekhara, M. S., Martin, P. B., and Tung, C. Compressible dynamic stall control using a variable droop leading edge airfoil, *Journal of Aircraft*, July-August 2004, **41**, (4), pp. 862-869.

16. Abbott, I. H., and von Doenhoff, A. E. *Theory of Wing Sections*, Dover, New York, 1959, pp. 111-115.

17. Peters, D. A., Barwey, D., and Su, A. An integrated airloads-inflow model for use in rotor a and control analysis, *Mathematical and Computer Modelling*, 1994, **19**, (3/4), pp. 109-123.

18. Peters, D. A., Johnson, M. Finite-state airloads for deformable airfoils on fixed and rotating wings, Symposium on Aeroelasticity and Fluid/Structure Interaction, American Society of Mechanical Engineers Winter Annual Meeting, November 1994.

19. Peters, D. A., and Karunamoorthy, S. State-space inflow models for rotor aeroelasticity, 12th AIAA Applied Aerodynamics Conference Proceedings, June 1994, pp. 828-837.